# Stochastic Localization of Microswimmers by Photon Nudging

**Andreas P. Bregulla,[†] Haw Yang,[‡] and Frank Cichos[†,*]**

[†]Molecular Nanophotonics Group, Institute of Experimental Physics I, University of Leipzig, 04103 Leipzig, Germany, and [‡]Chemistry Department, Princeton University, Princeton, New Jersey 08544, United States

**ABSTRACT** Force-free trapping and steering of single photophoretically self-propelled Janus-type particles using a feedback mechanism is experimentally demonstrated. Realtime information on particle position and orientation is used to switch the self-propulsion mechanism of the particle optically. The orientational Brownian motion of the particle thereby provides the reorientation mechanism for the microswimmer. The particle size dependence of the photophoretic propulsion velocity reveals that photon nudging provides an increased position accuracy for decreasing particle radius. The explored steering mechanism is suitable for navigation in complex biological environments and in-depth studies of collective swimming effects.

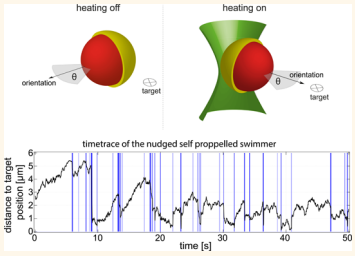


**KEYWORDS:** photophoresis · thermophoresis · microswimmer · Janus particle · trapping

Thermal fluctuations are omnipresent for particles and molecules in solution. They randomize positions and orientations and present a challenge to all attempts to manipulate and direct particle motion at the nano- and microscale. Swimmers or self-propelled particles are examples of how this Brownian motion can be overcome to cause directed motion. Such self-propelled motion has recently gained large interest, and a number of different propulsion mechanisms have been proposed.[1−7] Many of them are related to a phoretic swimming mechanism, which drives the particle due to an osmotic pressure difference along the particle surface. This phoretic propulsion creates a very special flow field,[8−10] where the motion of the particle essentially comes from a force balance between liquid and particle. The hydrodynamic boundary conditions at the swimmers surface and at the container walls drive the particle forward even though the system of particle and liquid is force free. When such self-propelled objects are starting to interact at higher densities, coherent collective motions are observed in which the swimmers align and form flocks, swarms, or other complicated patterns.[11−15] Dynamic clustering of active particles has been recently observed for chemically driven swimmers;[12,16] however, the details of this complex behavior are still not understood. The reason for this lack of understanding is partly due to the lack of control over the active particles itself. It is rather difficult to arrange active particles in clusters of well-defined size. Such control would allow a detailed study of active particle interactions resolving many details of their complex collective behavior. Since external force fields such as optical tweezers introduce additional mechanical forces to such particles, they completely change the hydrodynamic flow field of self-propelled particles and thus also their hydrodynamic interactions. A method to cluster particles in well-defined way to study their interactions thus has to preserve their hydrodynamic field correctly.

## PHOTON NUDGING

Recently, photon nudging has been proposed to control the self-propelled motion in an almost arbitrary way (see Figure 1).[17] The key ingredients for photon nudging are a switchable self-propelled motion of particles and an optical feedback of the particles position and orientation. Using this feedback, the propulsion engine of the particle can be switched on whenever the particles orientation is toward a target and off when not. Thus, self-propulsion leads to a localization of the active swimmer at a target location without the need for additional point forces of tweezers or external fields, which

* Address correspondence to cichos@physik.uni-leipzig.de.

Received for review March 20, 2014 and accepted May 26, 2014.

**Published online May 26, 2014**
**10.1021/nn501568e**

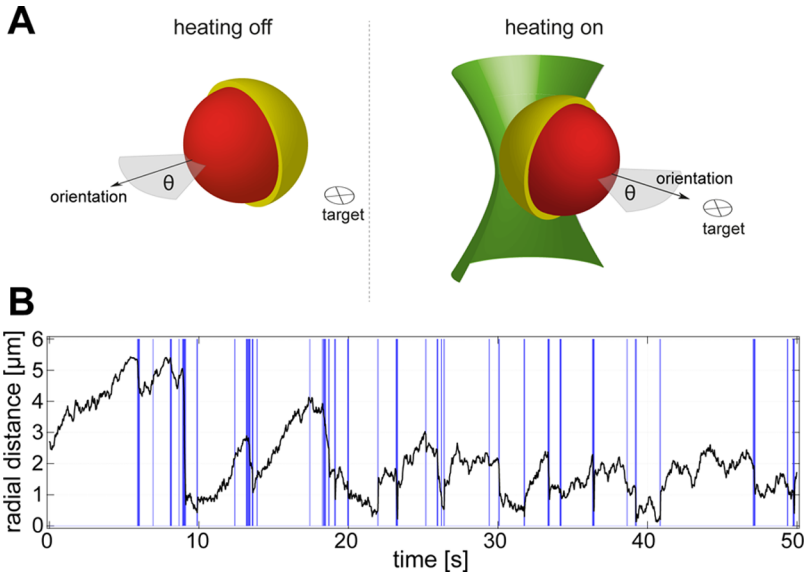


**Figure 1. (A) Schematic picture of the adaptive steering process. As long as the orientation of the particle with a certain acceptance angle $\theta$ does not point toward a defined target location the particle stays unheated. Brownian fluctuations reorient the particle, and its orientation eventually points toward the target and a propulsion mechanism is switched on. In the presented experiments, Janus particles are employed with the yellow color denoting a thin gold hemisphere on a polystyrene particle (red). (B) Representative experimental time trace showing the stochastic heating periods (blue bars) and the distance from the target (black line) for a Janus particle with a radius of $R$ = 0.625 $\mu$m ($\kappa$ = 1.33; $\lambda$ = 1.65).**

would distort the hydrodynamic field of the swimming objects. The general principle has been demonstrated by numerical simulations as well as by the first experiments.[17]

When the photon-nudging mechanism is turned on, the propulsion is switched on only when the particle is facing the target under an acceptance angle $\theta$ (*cf.* Figure 1A). Independent of whether the nudging is on or off, the rotational Brownian motion continues to randomly reorient the particle. The translational Brownian motion, on the other hand, will drive the particle away from its target location with high probability. Overall, the control strategy therefore only uses the propulsion for a small fraction of time, which is typically below 10% and which depends on the acceptance angle and the propulsion speed. Figure 1B displays an example time trace of heating pulses, with a minimum heating pulse duration corresponding to the inverse frame rate $\Delta t$.

The photon nudging concept leads to several new possibilities. One such possibility is stochastic localization. As mentioned earlier, the localization precision is a balance among the ubiquitous thermal fluctuations and the control parameters in an experiment. The positioning error for a photon nudged particle can be expressed as[17]

$$\sigma^2 = \langle |\vec{r}_t - \vec{r}_{\text{target}}|^2 \rangle_t \qquad (1)$$

which is measured as the time-averaged mean-squared distance of an active particle at $\vec{r}_t$ from its target position, $\vec{r}_{\text{target}}$. The time evolution of the radial distance $|\vec{r}_t - \vec{r}_{\text{target}}|$ of an active particle from its target position is displayed in Figure 1B and clearly reveals short periods of time (marked by the colored bars) during which the distance to the target decreases quickly. These periods correspond to the nudging action. The position error represents the stationary state of the radial distance of the particle from the target position. Two dimensionless control parameters have been identified through simulation studies:[17] The first parameter, the revolution number $\lambda$, measures the average number of rotations carried out by the particle within the experimental time scale $\Delta t$. An increasing $\lambda$ results in stronger randomization of the velocity direction during heating, which decreases the effective velocity of the particle along the direction toward the target. The second parameter, the propulsion number $\kappa$, reveals the relative persistence length, which denotes the propelled distance within the time period characteristic for the rotational diffusion time $\tau_R$ relative to the particle radius $R$:

$$\lambda = \frac{\Delta t}{\tau_R} \qquad (2)$$

$$\kappa = \frac{v_{\text{th}} \tau_R}{R} \qquad (3)$$

Furthermore, the simulation studies suggest that the position error in photon nudging decreases with the particle radius; that is, the smaller the particle, the better control photon nudging could achieve. Here we experimentally investigate the role of these control parameters in stochastic localization. As indicated in eqs 2 and 3, the particle radius, $R$, the experimental time scale (the inverse camera frame rate), $\Delta t$, and the nudging laser power which affect $v_{\text{th}}$ are

experimentally tunable variables that determine the control parameters, the revolution number $\lambda$, and the propulsion number $\kappa$.

The main contribution of this work is the experimental investigation of these parameters, confirming the theoretical and simulation predictions and providing for the first time a size-dependent study of the photophoretic (or self-thermophoretic) self-propulsion of Janus particles. We start by describing the size dependence of the propulsion mechanisms followed by summarizing a new implementation of photon nudging for 2D-confined Janus particles and a detailed presentation of the results.

## PROPULSION BY SELF-THERMOPHORESIS

The photon nudging concept relies on the capability of remotely switching on and off the self-propelling engine of the particle being steered. In the context of propulsion by local self-thermophoresis, a gold-capped polystyrene bead is irradiated by a laser. The energy absorbed by the gold cap is converted into heat and distorts the counterion cloud around the colloidal particle.[18,19] The resulting osmotic pressure difference across the particle induces a surface slip, which drives the particle at a velocity $\vec{v}_{th}$. In an experiment, the gold-coated hemisphere of a Janus particle would be heated by a 532 nm laser through plasmon-band absorption. The resulting photophoretic velocity, $\vec{v}_{th}$, is proportional to the temperature gradient $\vec{\nabla} T$ across the particle and its thermal diffusion coefficient $D_T$ by[2]

$$\vec{v}_{th} = -D_T \vec{\nabla} T \tag{4}$$

Experimentally, the photophoretic velocity is extracted directly from the photon-nudging time traces. It is the particle step within the time period in which the heating-laser is on projected onto the particle orientation divided by that time period.

The influence of the particle size on the propulsion velocity depends on the manner by which the temperature gradient $\vec{\nabla} T$ and the thermal diffusion coefficient $D_T$ vary with size. Let us consider the scenario that is consistent with the previous[17] and the current experiments, where the particle radius $R$ is much greater as compared to the gold layer with thickness $\Delta r$; that is, $R \gg \Delta r$ (see Figure 2 inset). In such a thin-cap limit and assuming that the thermal conductivity of the polymer particle $\kappa_i$ and the surrounding water $\kappa_o$ are approximately equal $\kappa_i \approx \kappa_o = \kappa_T$, the temperature distribution around the particle can be expanded into a series of Legendre polynomials and the temperature gradient along the particle surface $\vec{\nabla}_{||} T$ can be expressed as[8]

$$\vec{\nabla}_{||} T = \frac{1}{R}\frac{\partial T}{\partial \Theta}\vec{e}_\Theta = \frac{\Delta T}{R}\sum_{n=1}^{\infty} f_n \frac{dP_{2n-1}(\cos(\Theta))}{d\Theta}\vec{e}_\Theta \tag{5}$$

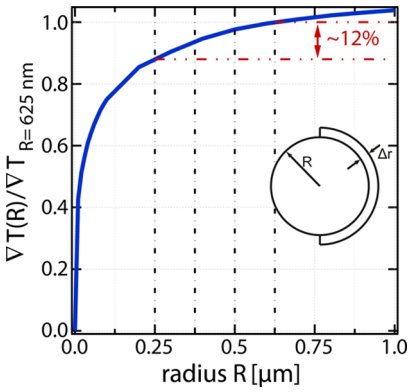


**Figure 2. Finite-element calculation of the relative temperature gradient (as compared to a $R = 0.625$ $\mu$m particle) at constant incident laser heating intensity as a function of particle radius $R$. The thickness of the metal cap $\Delta r$ has been kept constant. The relative gradient is found to be almost constant for particle radii above 0.25 $\mu$m (variation by less than 12%). The size range studied experimentally in this report is marked by the vertical dashed lines.**

where $\Theta$ in this equation is the polar angle from the Janus particle symmetry axis and $f_n$ is an angle independent prefactor arising in the Legendre expansion (see Supporting Information for details).The temperature rise $\Delta T$ in eq 5 is given by

$$\Delta T = \frac{\sigma_{abs} I_{inc}}{4\pi\kappa_T R} \tag{6}$$

where $\sigma_{abs}$ is the absorption cross section of the metal cap at the heating laser wavelength and $I_{inc}$ is the incident laser intensity. Finally, one arrives at a temperature gradient (see the Supporting Information for details)

$$\vec{\nabla}_{||} T \propto \frac{\sigma_{abs} I_{inc}}{R^2} \tag{7}$$

which is proportional to the absorption cross-section $\sigma_{abs}$ and inversely proportional to the square of the particle radius $R$. Furthermore, in the limit of $R \gg \Delta r$, we find that the gold cap volume $V = (2\pi/3)[(R + \Delta r)^3 - R^3]$ can be approximated by $V \approx 2\pi\Delta r R^2 \propto R^2$ and thus the absorption cross section scales with the particle radius squared $\sigma_{abs} \propto R^2$. Accordingly, the temperature gradient is expected to be linearly proportional to the incident laser power but independent of the particle radius in this thin cap limit. For smaller particle sizes, however, we expect eq 7 to be no longer valid. The absorption cross section will tend to a constant value as the particle radius $R$ approaches zero, in which case the cap resembles a half-sphere with radius $\Delta r$. The gradient will thus decrease for smaller particle sizes and finally tend to zero for $R = 0$.

To evaluate the influence of the above-mentioned assumption of a thin cap, we carried out finite-element simulations for a series of particles with different radius while keeping the metal cap thickness constant (COMSOL 4.2, see the Supporting Information for details). The result is shown in Figure 2. The simulation

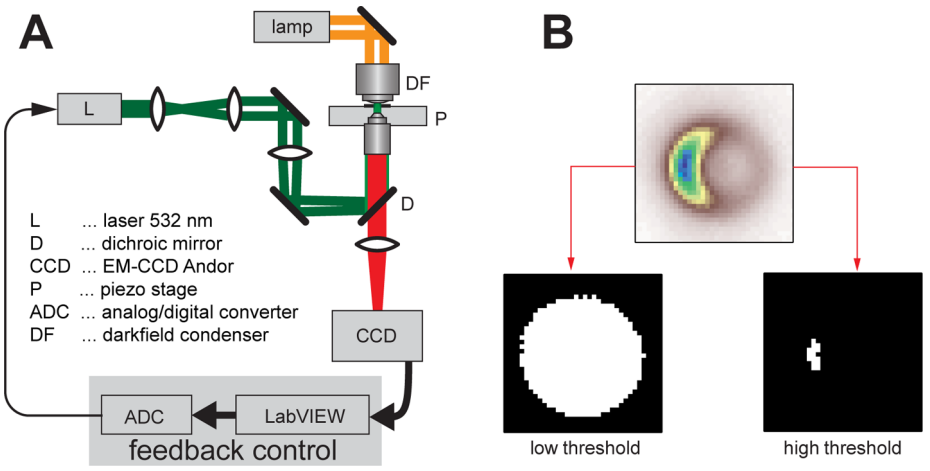


**Figure 3. (A) Schematics of the experimental setup. Main parts comprise the white light dark field illumination (yellow beam path), the laser excitation for optical heating (green beam path), and a detection element (red beam path) combined with a computer-assisted feedback mechanism. (B) Illustration of a typical experimentally acquired dark-field image of a Janus particle (top, false color) and the determination of the orientation by calculating the center of mass of a binary image done at low- (bottom left) and high-threshold (bottom right) values.**

suggests that the temperature gradient would drop by only 12% from $R = 0.625\ \mu$m particle to $R = 0.25\ \mu$m particle. Thus, the results of the analytical calculation presented above are approximately valid in the studied size range. However, when dropping to sizes below $R = 0.25\ \mu$m, the gradient quickly vanishes and the self-propulsion velocity decreases accordingly.

## EXPERIMENTAL SETUP

The experimental setup is schematically displayed in Figure 3A. It is different from the photon-nudging setup reported in ref 17. No real-time 3D single-particle tracking mechanism is required, since the particles are confined in a two-dimensional plane for long-time imaging and nudging. Because it is the first time that such a setup is presented, we briefly summarize the setup below. The Janus particles were observed using a dark-field illumination with an oil-immersion dark-field condenser (Olympus, NA 1.2−1.4). The scattered light of the particle was collected using a 100x oil-immersion objective (Olympus, adjustable NA 0.5−1.3). The numerical aperture of the microscope objective was set to be below the minimum aperture of the dark-field condenser. The scattered light was imaged to an EM CCD (Andor IXON). The total magnification microscopy setup was determined to be ~277. Dark-field images of the Janus particle were analyzed in real time with a LabView program. For each frame, two binary images were created. One at a low intensity threshold above the background noise and one at a high threshold typically at about 90% of the maximum intensity (Figure 3B). The center of mass of the binary image at low threshold determines the position of the particle. Together with the center of mass for the high-threshold image (position of the gold cap) the orientation of the particle was calculated.[17] This information was then sent to a real time measurement system

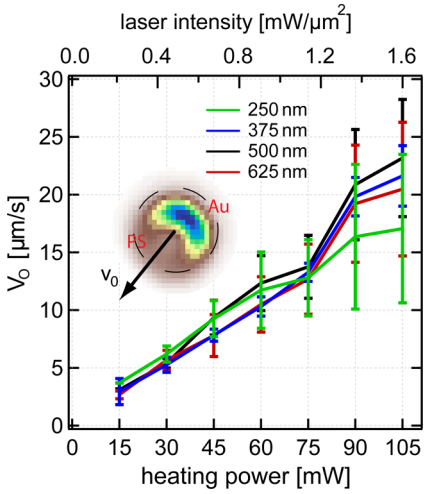


**Figure 4. Thermophoretic velocity as a function of the heating power for different particle sizes ($R = 0.25-0.625\ \mu$m). Besides the expected linear dependency on the heating power, the thermophoretic velocity does not depend on the particle radius.**

(ADWin Gold) to drive an acousto-optical deflector (Brimrose, 2DS-100−45−532) switching the wide field heating laser illumination (532 nm, Pusch Optotech) according to the orientation of the Janus particle with respect to the target. For all experiments reported here, the exposure time and the inverse frame rate of the camera were set to 15 ms.

## RESULTS AND DISCUSSION

Total of four Janus particles of diameter $R = 250$, 375, 500, and 625 nm were investigated. For all particle sizes, a linear increase of the velocity with the incident heating power was observed (see Figure 4). This is consistent with previous reports[2,17] and is due to the expected linear dependence of the temperature gradient $\nabla T$ on the incident heating power, *i.e.*, $\nabla T \propto \sigma_{abs} I_{inc}$ (see eq 7). The experimentally determined

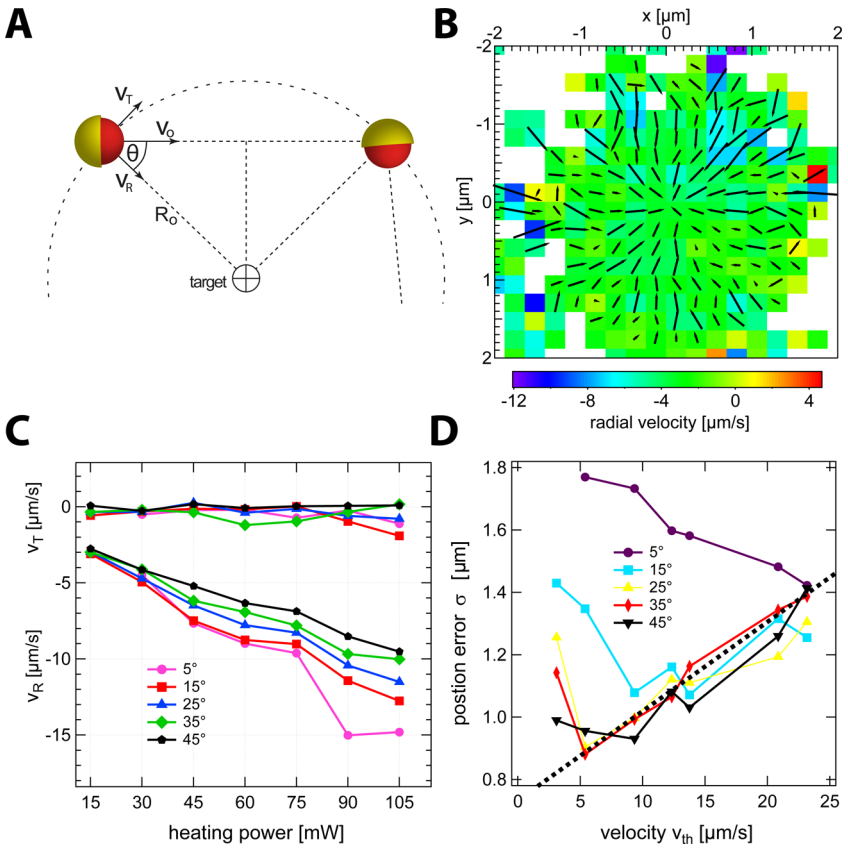


**Figure 5. Acceptance angle and laser heating powers. (A) Simple illustration of the particle's motion on a circle in the overcorrection regime due to the finite acceptance angle $\theta$. (B) Effective particle flow field with respect to the target at ($x = y = 0$ $\mu$m) during the stochastic localization process. The radial velocity magnitude is indicated by the color code, whereas the black arrows indicate the net direction and magnitude of the particle velocity $v_{th}$. (C) Time-averaged mean tangential and radial component of the particles propulsion with respect to the target position. (D) Dependence of the positioning error $\sigma$ on the heating power (velocity $v_{th}$) and acceptance angle $\theta$.**

propulsion direction is also in accord with the aforementioned ion cloud distortion mechanism, which causes a lower osmotic pressure at the heated gold cap. This osmotic pressure difference results in an ion flow from the cold to the hot side of the particle, which has to obey the no-slip boundary conditions at the particle and at the container surface; as a result, the flow propels the particle moving with the polymer side ahead. The strength of the thermo-diffusive effect is often measured relative to the diffusion coefficient $D$, which constitutes the Soret coefficient $S_T = D_T/D$. Since our experimental observation reveals an approximately constant velocity, $v_{th}$, under the same incident heating intensity and is nearly independent of the particle radius $R$, it follows that the thermal diffusion coefficient $D_T$ is independent of the particle size. This corresponds to a linear dependence of the Soret coefficient on the particle radius, $S_T \propto D_T/D \propto R$, in the size range studied here, which is consistent with recent reports.[20] During the photon-nudging process, the propulsion is now correlated with a specific orientation range of the Janus particle (see Figure 5A). This generates an effective particle flow toward the target as depicted in Figure 5B. The effective flow is the fundamental reason for a localization of the Janus particle at the target position. Even though the flow field is expected to have tangential components due to the finite acceptance angle, the tangential components are only persistent in direction for a time corresponding to the rotational diffusion time of the particle $\tau_R$. On longer time scales, the tangential components average to zero and a purely radial flow field remains (see Figure 5C). The displacement due to the effective radial flow during the propulsion periods competes with the translational Brownian motion. As described previously,[17] three different regimes are expected. The particle is weakly controlled at small velocities when the displacement by Brownian motion is still large as compared to the displacement by the propulsion. Thus, for decreasing propulsion velocity the position error $\sigma$ tends to infinity. As the velocity increases, the position error shall decrease and turn over into an overcorrection regime, where the increasing propulsion velocity is causing an overshoot beyond the target position. Figure 5D displays the experimental data revealing exactly this behavior exemplary for a particle of R = 0.5 $\mu$m and different acceptance angles $\theta$. A minimum position error is for example found for a

heating power of $P_{inc} = 30$ mW, which corresponds to a thermophoretic velocity of $v_{th} = 5\ \mu$m/s and an acceptance angle $\theta = 45°$. For smaller velocities, the displacement of the particle due to Brownian motion dominates the radial movements and the position error increases with decreasing velocity. In the overcorrected regime, the overshoot keeps the particle at a finite distance from the target and the distance increases linearly with increasing velocity. This overshoot distance can be calculated from simple geometric arguments as sketched in Figure 5A. The particle is propelled at the moment the edge of the acceptance angle $\theta$ is pointing toward the target location. In this moment, the velocity has an instantaneous radial and a tangential component driving the particle to a new position that is located on a circle with the radius $R_0 = v_{th}\Delta t/(2 \cos \theta)$. The position error for the particle is then determined by this overshoot distance and increases linearly with increasing velocity $v_{th}$ or heating power as visible in the experimental data in Figure 5D. The slope $m = \Delta t/2 \cos \theta$ of this linear increase with the particle velocity is determined by the heating time $\Delta t$ and the cosine of the acceptance angle $\theta$. The heating time is kept constant throughout our experiments. A change with the acceptance angle on the other side is expected but not observed in the experiment (see Figure 5D). We attribute this missing acceptance angle dependence to the experimental error in the determination of the particle orientation, *i.e.*, due to rotational motion during the exposure. If we assume and experimental error $\delta\theta$ in the determination of the particle orientation with respect to the target, the acceptance angle would effectively increase to $\theta_{exp} = \delta\theta + \theta$. This larger effective acceptance angle would increase the slope of linear increase of the overshoot distance with the particle velocity. From the linear part at high velocities in Figure 5C, we estimate the effective experimental acceptance angle $\theta_{exp}$ to be about 70°. Thus, the contribution of the experimental uncertainties to the acceptance angle are large and the defined acceptance angle becomes unimportant for the stochastic localization in 2D under the current experimental conditions.

**Optimal Control.** The nudging procedure will eventually lead to a stationary distribution of trajectory points around the target location with the width of the distribution characterized by the positioning error $\sigma$ defined earlier (*cf.* eq 1). Figure 6A summarizes the experimentally measured positioning error as a function of the control parameters, the revolution number $\lambda$, and the propulsion number $\kappa$ in a 2D contour plot, which contains all features presented above and allows some general conclusions. Figure 6A also compares nicely to our previous numerical results.[17] The slanted dotted line running from top left to bottom right indicates that the best localization in photon nudging is obtained for $\lambda \propto \kappa^{-2}$ as already reported earlier.[17] Our experimental results, however, reveal a smaller positioning error as expected. This is due to the fact that in the present experimental realization, the particles are confined between two glass slides. The confinement results in a lower diffusion coefficient of the particles due to the wall interaction.[21] The rotational diffusion, however, is not effected by the confinement due to the short-range hydrodynamic flow field associated with it. The measured translational diffusion coefficient corresponds to 25% of the Stokes−Einstein value. The lower diffusion coefficient will decrease the diffusive displacement during the time periods with no propulsion. This leads to a lower position error $\sigma$. On the other hand, this also requires a lower velocity to compensate for the diffusive displacement. Thus, the minima are also consistently found at lower values of $\kappa$ as compared to the numerical simulation data in ref 17. The corresponding rotational diffusion time $\tau_R$, which enters the calculations has been determined from the experimental data by autocorrelating the in plane particle orientation as reported in the supplement. Figure 2 of the supplement displays the corresponding measurement data and confirms the expected size dependence of the rotational diffusion time $\tau_R$.

We next discuss in more detail two different cases that are of interest for an experimental realization.

*Constant $\lambda$.* The first case is a constant revolution number $\lambda$. Here, the inverse frame rate of the experiment $\Delta t$ has to be scaled according to the rotational diffusion time $\tau_R$ of the particle. In this case, a well-defined value of $\kappa_{min}$ reveals the minimum in positioning error. A simple calculation shows that this requires the particle propulsion velocity (thus the incident heating power) to be scaled according to $v_{th} \propto 1/R^2$. Note that all of our experiments for one particle of radius $R$ correspond to this situation and the velocity at the minimum positioning error therefore reveals the value of $\kappa_{min}$. Parts B−D of Figure 6 display the corresponding particle trajectory points for the experiments with a heating time being 1/25 of the rotational diffusion time $\tau_R$ ($\log_{10}(\lambda) = -1.4$). As discussed earlier, the point cloud is extended in the case of small velocities (small $\kappa$) due to the dominance of Brownian motion. It reaches a minimum size for $\log_{10}(\kappa) = 0.6$ with $\log(\sigma/R) = 0.37$ (Figure 6C). This means that independent of the particle size, the localization error $\sigma$ is about 2.3 times the particle radius $R$. Small particles could thus be localized with much higher accuracy than larger ones. This is essentially due to the different scaling of the translational and rotational diffusion with the particle radius.[17] When further increasing the particle velocity the overcorrection regime is entered with a circular trajectory point distribution (Figure 6D).

Due to the required scaling of the velocity with the inverse particle radius and the shortening of the heating period $\Delta t$, this strategy becomes difficult to realize for small objects. Further, at very short heating

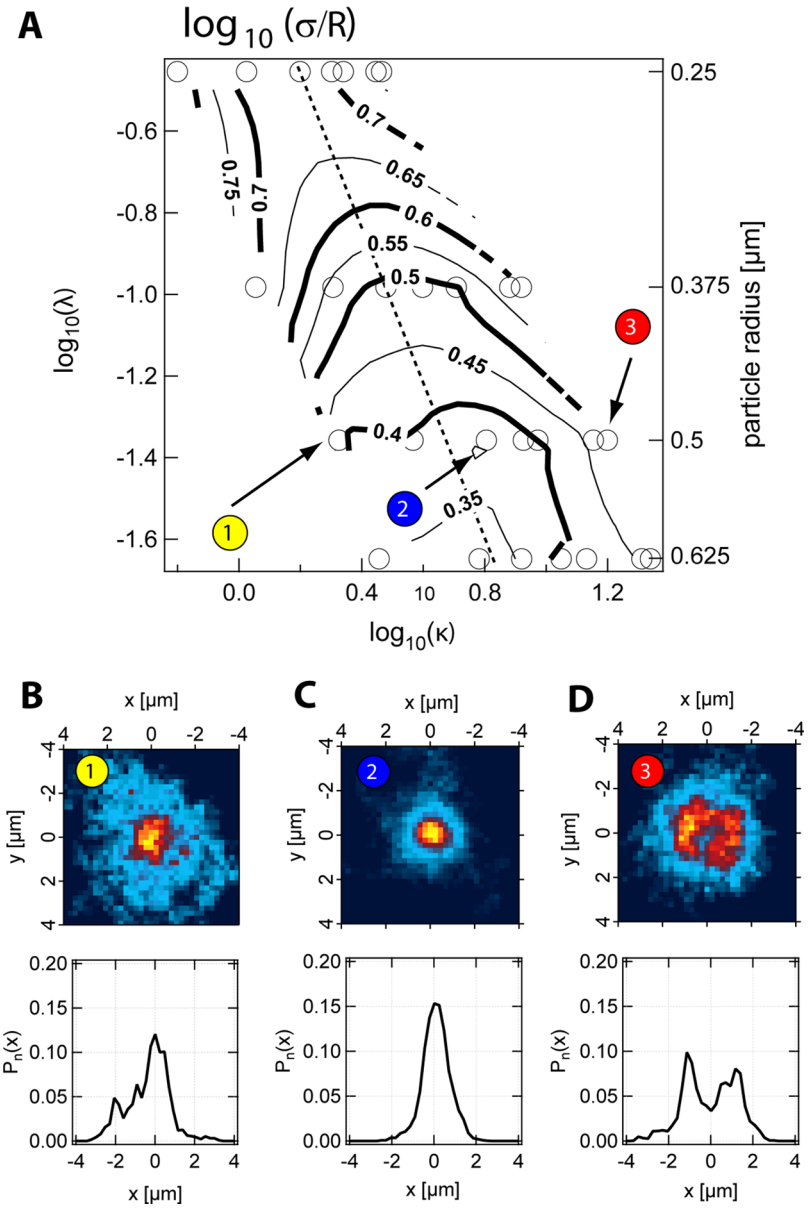


**Figure 6. Positional error in stochastic localization by photon nudging. (A) Summary of all experimental results for the relative positioning error $\sigma/R$ at the target position for particles of different radii $R$. The log of the relative position error is plotted as functions of the propulsion number $\kappa$ and the revolution number $\lambda$ (see eqs 2 and 3). (B–D) Examples of 2D probability distributions of the particle occurrence in the weakly controlled (B), the optimally controlled (C), and the overcorrection regimes (D).**

durations, the particle motion might show acceleration effects, which so far have not been explored in phoretic motion.

*Constant Frame Rate* $\Delta t$. A different approach would be to consider a constant inverse frame rate $\Delta t$. In this case, the revolution number $\lambda_{min}$ and the relative persistence length $\kappa_{min}$ are located along the dotted line in Figure 6A. Hence a thermophoretic velocity would have to be chosen according to

$$v_{th} \propto \frac{1}{\sqrt{R\Delta t}} \qquad (8)$$

which only scales with the inverse squared root of the particle size and thus requires much smaller heating powers to be applied for large particle sizes. However, since revolution number is not constant anymore, the positioning error $\sigma$ will depend on the revolution number $\lambda$. As displayed in Figure 6, the relative positional error $\sigma/R$ would then increase with increasing $\lambda$ or decreasing particle size. This approach would be suitable for slower camera-based photon-nudging implementations because the inverse frame rate of a typical camera is usually limited to tens of milliseconds. It provides a very easy way to control particles positions at good accuracy with an easy implementation, which could be, *i.e.*, advantageously used in drug delivery or microswimmer interaction studies.

## CONCLUSION

We have experimentally demonstrated the adaptive control of Janus particles of different size. The optically switchable photophoretic propulsion mechanism in conjunction with a feedback control based on particle orientations allows particle steering and trapping utilizing the orientational Brownian fluctuations of the particle. Our experimental results on Janus particles of different sizes reveal that the particle propulsion velocity is independent of the particle radius at constant incident heating intensity in the studied size range. The feedback controlled switching of the swimmer propulsion is employed to localize the particle at well-defined positions. The experimental positioning error displays two different regimes, where either diffusion or overcorrection due to large propulsion velocities dominate. The minimal positioning error decreases with decreasing particle size due to the stronger size dependence of the reorienting rotational Brownian motion. Two different control schemes with constant exposure and constant particle rotation number are discussed, which provide easy integration of the control strategy. Thus, photon nudging delivers a versatile tool for navigation in complex environments involving the navigation of propelled Janus particles labeled with sensor molecules or containing drugs within individual cells or the study of emergent phenomena of nonequilibrium dynamics of particles ensembles.

## MATERIALS AND METHODS

**Materials.** Janus particles have been prepared on standard microscopy glass coverslips, which have been treated in an oxygen plasma. A solution of polystyrene beads ($R = 0.25$, 0.375, 0.5, and 0.625 $\mu$m; Microparticles GmbH) is distributed on these coverslips in a spin coater at 8000 rpm. The particle concentration of the bead solution has been adjusted such that the particle do not form a closed packed monolayer but rather isolated particles. This reduces the number of aggregates formed during the gold layer depostion. The samples have been further covered with a 5 nm chromium and a 50 nm gold film by evaporation in a vacuum chamber. The chromium layer has been added to make sure that the gold layer adheres to the glass slide when removing the Janus particles from the glass substrate by sonification. Electron microscopy images of the resulting Janus particles of different size are displayed in the Supporting Information.

**Sample Preparation.** The samples for all photon nudging studies consist of two glass cover slides, which were rinsed with acetone, ethanol, and distilled water and treated with an oxygen plasma. They were further coated with Pluronic F-127 (Sigma-Aldrich) in a 5% aqueous solution for a few hours. The Pluronic was adsorbed to the glass surface and prevented sticking of the Janus particles to the glass surface due to electrostatic interactions. Residual Pluronic was removed by rinsing the coated slides with distilled water. A dilute Janus particle solution was then deposited between the two slides and sealed with polydimethylsiloxane (PDMS) to prevent evaporation of the aqueous solution. The typical thickness of the liquid layer between the glass slides was adjusted to be below 2 $\mu$m.

*Conflict of Interest:* The authors declare no competing financial interest.

*Acknowledgment.* We acknowledge help of M. Selmke concerning the temperature distribution around the Janus particles. We thank A. Würger and K. Kroy for helpful discussions. This work was financially supported by the Deutsche Forschungsgemeinschaft within the Collaborative Research Center SFB TRR-102.

*Supporting Information Available:* Detailed description of the derivation of the size-dependent surface temperature gradient in the thin cap limit as well as a description of the simulation of the temperature gradients. Three movies visualizing the different three trapping regions (undercontrolled, optimum control, overcontrolled). This material is available free of charge *via* the Internet at http://pubs.acs.org.

## REFERENCES AND NOTES

1. Dreyfus, R.; Baudry, J.; Roper, M. L.; Fermigier, M.; Stone, H. A.; Bibette, J. Microscopic Artificial Swimmers. *Nature* **2005**, *437*, 862–865.
2. Jiang, H.-R.; Yoshinaga, N.; Sano, M. Active Motion of a Janus Particle by Self-Thermophoresis in a Defocused Laser Beam. *Phys. Rev. Lett.* **2010**, *105*, 268302.
3. Wang, W.; Duan, W.; Ahmed, S.; Mallouk, T. E.; Sen, A. Small Power: Autonomous Nano- and Micromotors Propelled by Self-Generated Gradients. *Nano Today* **2013**, *8*, 531–554.
4. Gibbs, J.; Zhao, Y.-P. Autonomously Motile Catalytic Nanomotors by Bubble Propulsion. *Appl. Phys. Lett.* **2009**, *94*, 163104–163104.
5. Howse, J. R.; Jones, R. A.; Ryan, A. J.; Gough, T.; Vafabakhsh, R.; Golestanian, R. Self-Motile Colloidal Particles: From Directed Propulsion to Random Walk. *Phys. Rev. Lett.* **2007**, *99*, 048102.
6. Tierno, P.; Golestanian, R.; Pagonabarraga, I.; Sagués, F. Controlled Swimming in Confined Fluids of Magnetically Actuated Colloidal Rotors. *Phys. Rev. Lett.* **2008**, *101*, 218304.
7. Buttinoni, I.; Volpe, G.; Kümmel, F.; Volpe, G.; Bechinger, C. Active Brownian Motion Tunable by Light. *J. Phys.: Condens. Matter* **2012**, *24*, 284129.
8. Bickel, T.; Majee, A.; Würger, A. Flow Pattern in the Vicinity of Self-Propelling Hot Janus Particles. *Phys. Rev. E* **2013**, *88*, 012301.
9. Yang, M.; Ripoll, M. Thermophoretically Induced Flow Field around a Colloidal Particle. *Soft Matter* **2013**, *9*, 4661–4671.
10. Weinert, F. M.; Braun, D. Observation of Slip Flow in Thermophoresis. *Phys. Rev. Lett.* **2008**, *101*, 168301.
11. Schaller, V.; Weber, C.; Semmrich, C.; Frey, E.; Bausch, A. R. Polar Patterns of Driven Filaments. *Nature* **2010**, *467*, 73–77.
12. Palacci, J.; Sacanna, S.; Steinberg, A. P.; Pine, D. J.; Chaikin, P. M. Living Crystals of Light-Activated Colloidal Surfers. *Science* **2013**, *339*, 936–940.
13. Buttinoni, I.; Bialké, J.; Kümmel, F.; Löwen, H.; Bechinger, C.; Speck, T. Dynamical Clustering and Phase Separation in Suspensions of Self-Propelled Colloidal Particles. *Phys. Rev. Lett.* **2013**, *110*, 238301.
14. Cohen, J. A.; Golestanian, R.Emergent Comet-like Swarming of Optically Driven Thermally Active Colloids. **2013**, arXiv:1309.3318, *arXiv.org e-Print archive*.
15. Zhang, H.-P.; Beier, A.; Florin, E.-L.; Swinney, H. L. Collective Motion And Density Fluctuations in Bacterial Colonie. *Proc. Natl. Acad. Sci. U.S.A.* **2010**, *107*, 13626–13630.
16. Theurkauff, I.; Cottin-Bizonne, C.; Palacci, J.; Ybert, C.; Bocquet, L. Dynamic Clustering in Active Colloidal Suspensions with Chemical Signaling. *Phys. Rev. Lett.* **2012**, *108*, 268303.
17. Qian, B.; Montiel, D.; Bregulla, A.; Cichos, F.; Yang, H. Harnessing Thermal Fluctuations for Purposeful Activities: the Manipulation of Single Micro-swimmers by Adaptive Photon Nudging. *Chem. Sci.* **2013**, *4*, 1420–1429.

18. Dhont, J.; Briels, W. Single-Particle Thermal Diffusion of Charged Colloids: Double-Layer Theory in a Temperature Gradient. *Eur. Phys. J. E Soft Matter* **2008**, *25*, 61–76.
19. Würger, A. Thermal Non-equilibrium Transport in Colloids. *Rep. Prog. Phys.* **2010**, *73*, 126601.
20. Braibanti, M.; Vigolo, D.; Piazza, R. Does Thermophoretic Mobility Depend On Particle Size? *Phys. Rev. Lett.* **2008**, *100*, 108303.
21. Kihm, K.; Banerjee, A.; Choi, C.; Takagi, T. Near-wall Hindered Brownian Diffusion of Nanoparticles Examined by Three-dimensional Ratiometric Total Internal Reflection Fluorescence Microscopy (3-D R-TIRFM). *Exp. Fluids* **2004**, *37*, 811–824.